



A joint seismic and acoustic study of the Washington State bolide: Observations and modeling

Stephen J. Arrowsmith,^{1,4} Douglas P. Drob,² Michael A. H. Hedlin,¹ and Wayne Edwards³

Received 5 September 2006; revised 8 December 2006; accepted 25 December 2006; published 3 May 2007.

[1] On 3 June 2004, a bolide was observed over British Columbia, Washington, Oregon, and Idaho. In addition to eyewitness accounts, the event was recorded on videotape and at ~ 100 seismometers located in Washington State and southern British Columbia. Seismic records are consistent with a terminal burst rather than the hypersonic shock of the meteors passage through the atmosphere. Arrival times from seismic waveform data are used to obtain an accurate source location for this terminal burst. The source location can effectively be considered to be ground-truth for assessing current atmospheric models and infrasound propagation algorithms. We observe clear infrasonic signals associated with the terminal burst of the fireball at infrasound stations I56US and I57US in Washington State and California, respectively. At I56US we observe at least four distinct acoustic arrivals, for which we are able to model three using a state-of-the-art atmospheric model (the Ground-to-Space (G2S) model) and both ray-tracing and parabolic equation propagation algorithms. To our knowledge, this is the first study in which a complex sequence of arrival packets at an individual station has been successfully modeled by range-dependent ducting and specular reflection off terrain gradients. At I57US a single coherent acoustic signal was observed, which we are unable to satisfactorily model. This could be due to errors in the specification of the background atmosphere, incorrect assumptions and approximations inherent to the acoustic propagation algorithms, and the greater range of propagation, which amplifies the effect of errors in source location and the atmospheric specifications.

Citation: Arrowsmith, S. J., D. P. Drob, M. A. H. Hedlin, and W. Edwards (2007), A joint seismic and acoustic study of the Washington State bolide: Observations and modeling, *J. Geophys. Res.*, *112*, D09304, doi:10.1029/2006JD008001.

1. Introduction

[2] Bolides entering the Earth's atmosphere generate infrasound signals that can be detected using acoustic arrays over large distances [Revelle, 1976; Evers and Haak, 2001; Brown et al., 2002; Brown et al., 2003; Brown et al., 2004; Le Pichon et al., 2002a; Evers and Haak, 2003]. In addition, the sonic booms caused by bolides impacting the atmosphere at hypersonic velocities cause ground-coupled acoustic waves, which can be measured using seismic arrays. Seismic detections of bolides have been observed by Anglin and Haddon [1987], Qamar [1995], Ishihara et al. [2003], and Langston [2004].

[3] With the development of the International Monitoring System (IMS) infrasound array for use in monitoring the Comprehensive Nuclear-Test-Ban Treaty (CTBT), scientific investigation of ground-truth infrasound events is required

in order to validate atmospheric models and to test propagation codes. Unlike in seismology, where numerous events can be used to test and refine models of the Earth's crust and mantle, the infrasound community relies on relatively few events. One of the most important types of event in this regard is the large meteoroids (0.1–10 m in diameter). These bolides often explode high in the atmosphere at elevations between 15 and 40 km [McIntosh, 1970], generating infrasound signals that can be observed over a large range.

[4] The Washington State bolide occurred on 3 June 2004 and was visibly observed over British Columbia, Washington, Oregon, and Idaho. The event was recorded by a number of seismometers located in Washington State and British Columbia and by a Sandia all-sky camera located in British Columbia. The numerous seismic observations of this event provide us with an opportunity to obtain a source location with a high degree of certainty. The seismic observation can effectively be considered to be ground-truth for assessing the accuracy of the infrasound location because the certainty of the seismic location is much better than the infrasound, in part due to the larger ranges of the infrasound sensors. Therefore the Washington State bolide provides us with a good opportunity to validate and to test atmospheric models and

¹Institute of Geophysics and Planetary Physics, Scripps Institution of Oceanography, University of California, San Diego, California, USA.

²U.S. Naval Research Laboratory, Washington, DC, USA.

³Department of Earth Sciences, University of Western Ontario, London, Ontario, Canada.

⁴Now at Los Alamos National Laboratory, EES-2, Los Alamos, NM, USA.

Table 1a. PNSN and USNSN Seismic Observations

Station	Latitude (°N)	Longitude (°W)	Elevation (km)	Arrival 1	Arrival 2	Waveform Type
ACES ^a	47.5597	122.3399	0.000	227.30	–	–
ASR	46.1528	121.6004	1.357	690.22	–	Impulsive
ATES ^a	48.2364	122.0592	0.062	175.07	–	–
BABE ^a	47.6058	122.5353	0.083	240.07	–	–
BEVT ^a	47.9200	122.2700	0.170	160.72	–	–
BLN	48.0074	122.9718	0.585	280.47	–	Reverberatory
BOW	46.4750	123.2281	0.87	626.38	–	Dispersed
BRKS ^a	47.7553	122.2883	0.020	180.42	–	–
CMW	48.4237	122.1190	1.19	222.39	–	Impulsive intermediate
CPW	46.9738	123.1363	0.792	477.84	–	Dispersed
EARN ^a	47.7409	122.0438	0.159	165.62	–	–
EGRN ^a	47.0733	122.9781	0.057	431.24	–	–
ELW	47.4943	121.8714	0.267	228.39	–	Reverberatory
ERW	48.4540	122.6251	0.389	277.29	–	Dispersed
EVCC ^a	48.0075	122.2043	0.030	153.33	–	–
EVGW ^a	47.8544	122.1534	0.122	153.82	–	–
FINN ^a	47.7195	122.2322	0.121	181.02	–	–
FL2	46.1964	122.3503	1.378	732.39	–	Dispersed
FMW	46.9416	121.6698	1.859	419.73	–	Dispersed
GMW	47.5479	122.7863	0.506	290.71	292.91	Impulsive
GNW	47.5644	122.8253	0.165	293.88	295.68	Impulsive
GSM	47.2032	121.7945	1.305	320.54	325.76	Dispersed
HDW	47.6485	123.0542	1.006	318.87	320.00	Impulsive
HICC ^a	47.3901	122.2979	0.115	269.89	–	–
HSR	46.1744	122.1794	1.720	667.19	–	Dispersed
HTW	47.8039	121.7676	0.833	161.10	–	Reverberatory
JCW	48.1952	121.9253	0.792	164.34	–	Reverberatory
KDK ^a	47.5952	122.3322	0.004	217.97	–	–
KICC ^a	47.5772	122.6312	0.017	262.27	–	–
KIMB ^a	47.5748	122.3028	0.069	219.79	–	–
KIMR ^a	47.5031	122.7672	0.123	296.92	–	–
KINR ^a	47.7517	122.6431	0.008	232.57	–	–
KITP ^a	47.6750	122.6297	0.076	241.49	–	–
LCW	46.6707	122.7008	0.396	522.93	528.67	Dispersed
LEOT ^a	47.7679	122.1156	0.115	163.72	–	–
LMW	46.6680	122.2913	1.195	503.47	506.05	Reverberatory
MARY ^a	47.6627	122.1199	0.011	185.44	–	–
MBKE ^a	48.9172	122.1414	1.010	375.68	–	–
MBW	48.7840	121.8997	1.676	331.25	334.69	Dispersed
MCW	48.6792	122.8314	0.693	356.55	357.65	Impulsive intermediate
MEAN ^a	47.6227	122.3052	0.037	208.49	–	–
MEW	47.2019	122.6458	0.098	359.82	–	Dispersed
NIHS ^a	47.7414	122.2214	0.137	175.92	–	–
NLO	46.0894	123.4505	0.826	760.71	–	Dispersed
OBC	48.0353	124.0775	0.938	490.28	–	Impulsive
OCWA	47.7489	124.1781	0.671	517.50	–	Impulsive
OFR	47.9333	124.3947	0.152	554.46	556.06	Dispersed
OHC ^a	47.3339	123.1581	0.006	393.23	–	–
OPC	48.1003	123.4116	0.090	365.82	–	Impulsive intermediate
PCFR ^a	46.9898	122.4409	0.137	405.68	–	–
PCMD	46.8891	122.3003	0.239	426.58	431.83	Dispersed
PNLK ^a	47.5818	122.0336	0.128	202.73	–	–
QAW ^a	47.6318	122.3543	0.140	211.62	–	–
RCS	46.8710	121.7311	2.877	436.85	440.16	Dispersed
RHAZ ^a	47.5402	122.1837	0.108	219.85	–	–
RMW	47.4597	121.8053	1.024	240.25	252.54	Reverberatory
RPW	48.4483	121.5136	0.850	255.14	266.50	Reverberatory
RRHS	46.7996	123.0404	0.047	513.52	–	Dispersed
RVW	46.1481	122.7423	0.460	690.61	699.74	Dispersed
SBES	48.7683	122.4151	0.119	341.72	–	Impulsive
SCC ^a	47.7498	122.3598	0.000	189.42	–	–
SEA	47.6544	122.3081	0.030	370.26	391.62	Impulsive
SEP	46.2002	122.1911	2.116	662.03	–	Dispersed
SLF	47.7589	120.5278	1.750	393.49	408.60	Reverberatory
SNB ^a	48.7760	123.1712	0.408	422.625	–	–
SOS	46.2440	122.1367	1.270	644.97	654.65	Dispersed
SQM	48.0775	123.0456	0.030	297.04	302.78	Reverberatory
STD	46.2378	122.2228	1.268	650.72	657.74	Dispersed
SVOH	48.2894	122.6319	0.022	245.57	–	Reverberatory
SVTR ^a	47.4959	121.7804	0.146	232.02	–	–
SWID ^a	48.0086	122.4117	0.062	179.02	–	–
TDL	46.3508	122.2158	1.400	613.33	615.05	Dispersed
TTW	47.6946	121.6889	0.542	188.59	–	Reverberatory

Table 1a. (continued)

Station	Latitude (°N)	Longitude (°W)	Elevation (km)	Arrival 1	Arrival 2	Waveform Type
UWFH ^a	48.5461	123.0119	0.010	351.32	–	–
VDB ^a	49.0261	122.1028	0.404	416.48	–	–
VVHS ^a	47.4236	122.4536	0.095	274.28	–	–
WISC ^a	47.6089	122.1744	0.056	201.57	–	–
WPW	46.6988	121.5361	1.280	507.04	509.77	Dispersed
WRW	47.8572	120.8811	1.189	310.95	–	Reverberatory
YEL	46.2097	122.1878	1.750	658.98	–	Dispersed

^aArrival times from initial University of Washington analysis.

propagation codes designed for the study of infrasound propagation.

[5] In this paper, we begin by discussing the seismic observations of the air-to-ground-coupled infrasound. We use the seismic data to obtain a source location with a high degree of certainty. Next, we discuss the infrasound observations from the Washington State bolide, which was recorded at two International Monitoring System (IMS) infrasound arrays: I56US and I57US, located in eastern Washington State and southern California, respectively. We then compare our observations with synthetic results obtained by forward modeling the propagation of infrasound using detailed atmospheric models and both ray-tracing and parabolic equation (PE) propagation codes. Our aim is to assess the state-of-the-art in infrasound modeling capabilities. We attempt to accurately model the propagation of infrasound in order to explain the complex waveform signatures recorded at I56US and I57US, providing an assessment of current understanding and implementation of infrasound propagation physics.

2. Seismic Observations

[6] The airwaves generated by the bolide were of sufficient energy to be recorded on nearly 100 seismometers located in Washington State and southern British Columbia, covering an area of $\sim 75,000$ km². Therefore this event comprises perhaps the largest number of seismic observations of a bolide to date (Tables 1a and 1b). The bulk of the observa-

tions (80 stations) are from the Pacific Northwest Seismic Network (PNSN) and the U.S. National Seismic Network (USNSN), while the remainder were recorded by the Canadian National Seismic Network (CNSN, 7 stations) and the western arm of the Portable Observatories for Lithospheric Analysis and Research Investigating Seismicity (POLARIS) Consortium broadband seismic network (12 stations). Of these observations, we were able to obtain digital waveforms for 64 stations. Though we could not obtain waveform data for the remaining stations, arrival times were obtained from a preliminary analysis performed by the University of Washington (S. Malone, personal communication, 2004).

[7] We have grouped the observed waveforms into four categories of seismo-acoustic response, which are described below with examples given in Figure 1. The variation in seismic amplitudes between stations should be noted. This is strongly related to the type of material the station is situated upon, and thus the coupling efficiency of the airwave with the surface. However, here we focus on the arrival time observations, and therefore a detailed discussion of the seismic amplitudes is beyond the scope of this text.

[8] (1) Impulsive: A brief high-amplitude initial response with a rapid return to presignal noise levels, typically with durations <10 s.

[9] (2) Impulsive intermediate: Similar to an impulsive-type response, these waves show a sharp high-amplitude initial response, approximately <10 -s duration; however, this is soon followed by a broad dispersed pulse often lasting for several tens of seconds.

Table 1b. POLARIS and CNSN Seismic Observations

Station	Latitude (°N)	Longitude (°W)	Elevation (km)	Arrival 1	Arrival 2	Waveform Type
ANMB	49.3187	–122.8585	0.179	540.52	–	Impulsive intermediate
COQB	49.3542	–122.7747	0.161	546.82	–	Impulsive
ENGB	49.0080	–123.0889	0.055	471.38	482.15	Dispersed
GOBB	48.9493	–123.5105	0.161	507.27	510.24	Impulsive
HBDB	49.1697	–122.2135	0.006	325.92	458.90	Dispersed
HNB	49.2744	–122.5792	0.185	509.65	–	Impulsive
KHVB	48.5688	–123.4663	0.041	425.02	–	Impulsive intermediate
MGCB	48.6317	–123.6808	0.236	469.23	–	Impulsive intermediate
PGC	48.6500	–123.4508	0.005	437.02	–	Dispersed
PIMB	49.2743	–122.6661	0.043	513.44	514.98	Dispersed
SHVB	48.4723	–123.6360	0.041	2074.7	395.97	Impulsive intermediate
SILB	48.6020	–123.2815	0.076	401.88	403.94	Impulsive intermediate
SNB	48.7750	–123.1708	0.405	422.60	–	Impulsive intermediate
SSIB	48.7558	–123.3875	0.012	448.50	449.85	Impulsive intermediate
TSJB	48.6013	–123.9885	0.378	516.55	517.96	–
TWBB	48.5846	–124.0920	0.122	533.00	562.85	Impulsive intermediate
TWGB	48.6076	–124.2559	0.127	565.46	–	Impulsive
TWKB	48.6449	–123.7332	0.128	480.19	481.33	Impulsive intermediate
VGZ	48.4139	–123.3244	0.068	377.90	–	Reverberatory

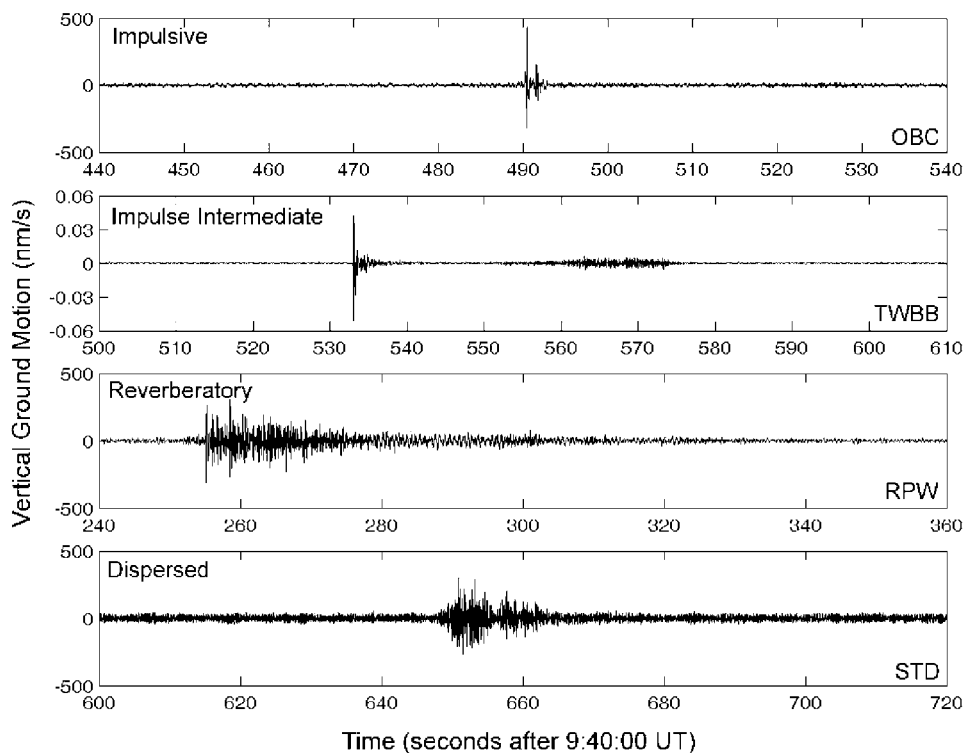


Figure 1. Examples of classification scheme of waveforms observed from the 3 June 2004 bolide.

[10] (3) Reverberatory: Rapid high-amplitude initial response followed by a train of slowly decaying reverberations lasting up to ~ 80 s in duration.

[11] (4) Dispersed: Showing no sign of the distinct onset of the previous three categories, these waves instead ramp up to a peak in amplitude then decay away in a more drawn-out, pulse-like response.

[12] Arrival times for these observations were picked from the initial onset of the wave packet, often in the form of a distinct negative ground motion, signifying the arrival of the positive overpressure of the airwave. This is a common feature often seen in other seismic observations of meteor and other airborne sources [e.g., Langston, 2004; Ishihara *et al.*, 2004; Cates and Sturtevant, 2002]. In the case of dispersed responses, arrival times were chosen at the onset of the maximum amplitude of the waveform. Arrival times and categories of seismic responses are given in Tables 1a and 1b.

3. Location

[13] By mapping the arrival time picks we observe nearly circular isochrones (Figure 2), which suggests that the source of the signals is from a point-like impulse. This implies that the origin of the signals is associated with the bolide's terminal burst rather than the hypersonic shock produced by the meteoroid's high-speed passage through the atmosphere. The latter type of origin would have produced hyperbolic isochrones [e.g., Ishihara *et al.*, 2004]. A terminal burst, the result of catastrophic fragmentation of the meteoroid, often occurs at a position near the end of a fireball's luminous trajectory and results in a dramatic increase in its brightness. Such a peak in bright-

ness was observed for the Washington State bolide at a single all-sky camera in Courtenay, British Columbia (49.6768°N , 125.0101°W). Timing of the burst was recorded by video time stamp to be at 9:40:14 UT, though subsequent calibration using a GPS clock showed this time to be in error of $+2$ s, placing the origin time of the burst at $9:40:12.0 \pm 0.3$ s. The error of ± 0.3 s denotes the estimated accuracy with which the time stamp was visually adjusted to the correct (GPS) time.

[14] In this study, we utilize the Naval Research Laboratory (NRL) Ground-to-Space (G2S) model, discussed by Drob *et al.* [2003] and Drob [2004], to provide background atmospheric information for calculating the source location from the seismic records and for forward modeling simulations of infrasound propagation (see later section). These specifications are based on operational lower atmospheric numerical weather prediction analysis fields below 55 km and the NRLMSISE-00/HWM-93 empirical upper atmospheric models above 55 km. The event-driven G2S data processing system was used to combine available operational troposphere/stratosphere numerical weather prediction (NWP) specifications from NOAA [Kanamitsu, 1989; Kalnay *et al.*, 1990] and NASA [Bloom *et al.*, 2005] with the NRLMSISE-00/HWM-93 [Picone *et al.*, 2002; Hedin *et al.*, 1996] upper atmospheric empirical models. This system spectrally combines $1^{\circ} \times 1^{\circ}$ and $1^{\circ} \times 1.25^{\circ}$ resolution global NWP input fields to the nearest 6-hour interval in the lower atmosphere with NRLMSISE-00/HWM-93 empirical model output to the nearest UT hour. The resulting specifications resolve the hourly variation of the upper atmospheric solar migrating tidal components, as well as the synoptic meteorology in the troposphere and stratosphere.

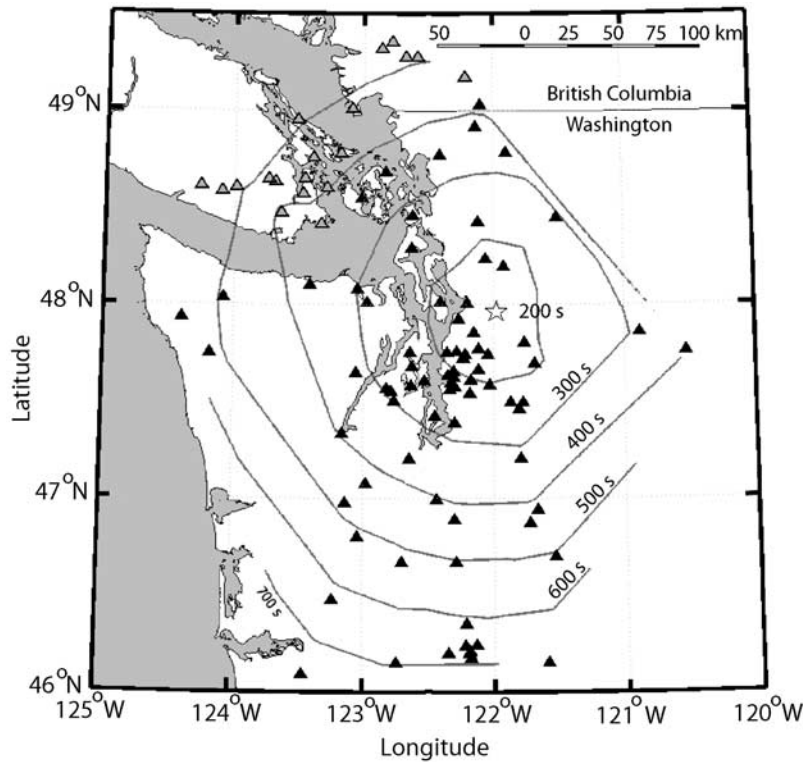


Figure 2. Observing stations and the main terminal burst location (star) of the 3 June 2004 bolide. Black and gray triangles indicate PNSN/USNSN and POLARIS/CNSN seismic stations, respectively.

[15] Using all 99 observed seismic arrival times initially, and the G2S atmospheric model used later for infrasonic propagation modeling, the location of the terminal burst in the atmosphere was located using the SUPRACENTER atmospheric explosion location program [Edwards and Hildebrand, 2004] and is given in Table 2 and shown as the “star” in Figure 2. The SUPRACENTER location algorithm uses a nonlinear, genetic optimization algorithm to quickly sample and determine the point source position. The algorithm yields a global minimum in traveltimes by discarding those observations determined (by ray tracing) not to be direct arrivals. The final solution uses 43 of the 99 initial arrival times and has a mean absolute traveltimes residual of 1.09 ± 2.08 s, from stations primarily within 70 km of the solution epicenter, a distance marking the onset of geometric refraction of acoustic paths back into the stratosphere. This position of the bolide’s terminal burst is well constrained in the horizontal plane by the many single vertical component seismometers surrounding the city of Seattle. Altitude, however, was found to be very sensitive to the origin time, with a computed uncertainty (increase in the mean traveltimes residual from the global minimum) in altitude of ± 7 km associated with an uncertainty in the origin time of ± 1.6 s. Timing at the closest stations surrounding the terminal burst (within 25 km of the epicenter) arrives much too soon/late if the uncertainty in altitude is indeed this large due to slow (~ 300 m/s) acoustic speeds, with closer station arrivals suffering at the expense of fitting more distant observations. Thus based on the closer observations, a better estimate of the uncertainty in altitude is closer to ± 1 km. Despite issues with the magnitude of uncertainty in altitude, this positioning places the

terminal burst ~ 10 km ENE of the city of Snohomish, WA, and agrees well with both the timing and direction of the terminal burst as seen by the all-sky camera.

[16] Further examination of the seismic records reveals that nearly half (31) of the seismic waveforms, mostly occurring at stations >90 km distant, show indications of a second airwave arrival, possibly a second fragmentation event. Surprisingly, the second arrival is not present at much closer stations, suggesting that either this is a type of acoustic reflection or the two fragmentations were spatially close together. If the latter is the case, then at close range the two acoustic pulses may have been nearly indistinguishable and so appear as one, while at greater distances the slightly different propagation paths have allowed the two airwaves to separate. Unfortunately, the generally large distances of the second set of arrivals make the uncertainty in the position of this second point source large, such that it is difficult to distinguish a second event from the main terminal burst.

[17] Aligning the observations with respect to the range from the terminal burst (Figure 3), it becomes clear that the seismic waves are propagating at near surface acoustic

Table 2. Terminal Burst Location for the 3 June 2004 Bolide as Determined by Seismic Arrival Times of the Airwave

	Location	Uncertainty
Latitude	47.96°N	$\pm 0.02^\circ$
Longitude	121.976°W	$\pm 0.002^\circ$
Altitude	39.3 km	± 7 km (± 1.0)
Origin Time	09:40:13.6 UT	± 1.6 s

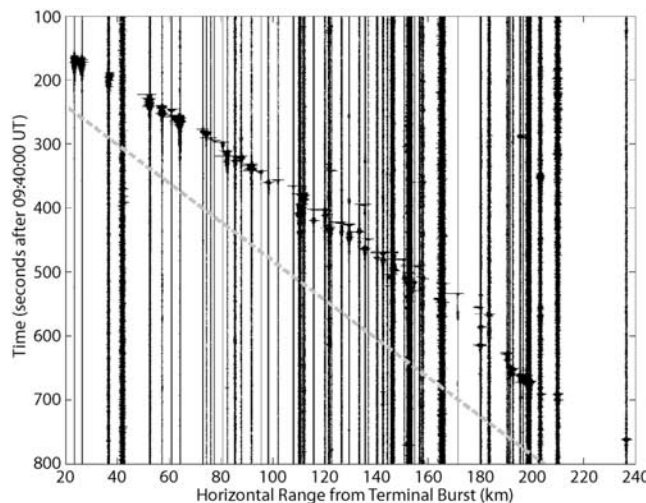


Figure 3. Seismic detections of the 3 June 2004 bolide terminal airburst as it propagated across northwestern Washington and southern British Columbia. A slope of 330 m/s is shown by the dashed gray line, given for reference.

velocities; approximately 330 m/s. This is somewhat unusual as many observations are located in areas where zones of silence are predicted based on atmospheric models. Possible explanations for the observed seismic energy within these “silent zones” are the nonlinear atmospheric dispersion of the airwave, trapping, and scattering of the acoustic energy in the lower atmosphere by unresolved mesoscale variations and fine-scale structure and complex atmospheric–seismic coupling effects in a terrain-rich environment.

4. Infrasound Observations

[18] The Washington State bolide was recorded at the I56US and I57US infrasound arrays, which are part of the IMS infrasound network. The I56US array, which is located 363 km from the terminal burst of the bolide, consists of four microbarometers with an aperture of 1.5 km. I57US, located at a range of 1659 km from the terminal burst of the bolide, consists of eight microbarometers with an aperture of 2 km. Each microbarometer is fitted with a rosette filter to reduce atmospheric noise [Hedlin *et al.*, 2003]. The Progressive Multi-Channel Correlation (PMCC) algorithm [Cansi, 1995] is applied to the data recorded at each station separately in order to identify and characterize signals consistent on all array elements. For a full description of the PMCC algorithm, the reader is referred to Cansi [1995]. Briefly, the basis of the PMCC algorithm is a measure of signal consistency (r_{ijk}), computed between a subnetwork of three proximate array elements (i, j, k), defined by the closure relation,

$$r_{ijk} = \Delta t_{ij} + \Delta t_{jk} + \Delta t_{ki},$$

where Δt_{ij} is the time delay between the arrival of a signal at sensors i and j , computed for each pair of traces using the cross-correlation function. We filtered the data using a Chebyshev filter with a passband from 0.05 to 2 Hz in order to remove low- and high-frequency noise. A threshold maximum consistency of 0.5 s was defined for the detection

of a waveform consistent on all the array elements. Starting from the initial subnetwork, a guided search of the wave parameters is performed. While the consistency is lower than the threshold, the detection is extended by including other array elements using the last propagation information calculated. This avoids ambiguity problems inherent in correlating distant signals. This analysis is performed in 10 frequency bands and a series of overlapping windows in time (length = 40 s, overlap = 10 s). Each elementary detection is then associated with the following parameters: (1) the number of sensors for which the consistency relation holds, (2) the associated consistency, (3) the mean cross-correlation coefficient, (4) the RMS amplitude of the waveform, (5) the apparent horizontal velocity, and finally (6) the azimuth of the incoming wavefront. A nearest neighbor search method is then used to cluster elementary detections into families associated with the coherent detected waveforms.

[19] Figure 4 shows the acoustic signals that were detected at I56US and I57US, respectively, with associated derived parameters from applying the PMCC algorithm. The main characteristics of the signals are given in Table 3. A map that shows the cross bearings of the two signals observed at I56US and I57US is plotted in Figure 5. The signal backazimuths agree well with the seismically derived location, providing good confidence that they are associated with the same source. At I56US there is evidence for at least four (and possibly five) distinct arrivals that occur over a period of approximately 8.5 min, starting at 09:59 GMT. The signals come from an azimuth of $263.1 \pm 2.8^\circ$ with speeds of 335–357 m/s. Arrival D (Figure 4), which contains the largest amplitudes, is notably of a much lower frequency than the earlier signals. At I57US we observe a single long-duration (~ 9 min), highly correlated waveform rather than separate arrivals as observed at I56US. The signals come from an azimuth of $345.7 \pm 2.5^\circ$ with speeds of 344–368 m/s. We note significant increases in the trace velocity (390–400 m/s) at $\sim 11:12$ and $\sim 11:21$. The largest signal amplitudes occur between

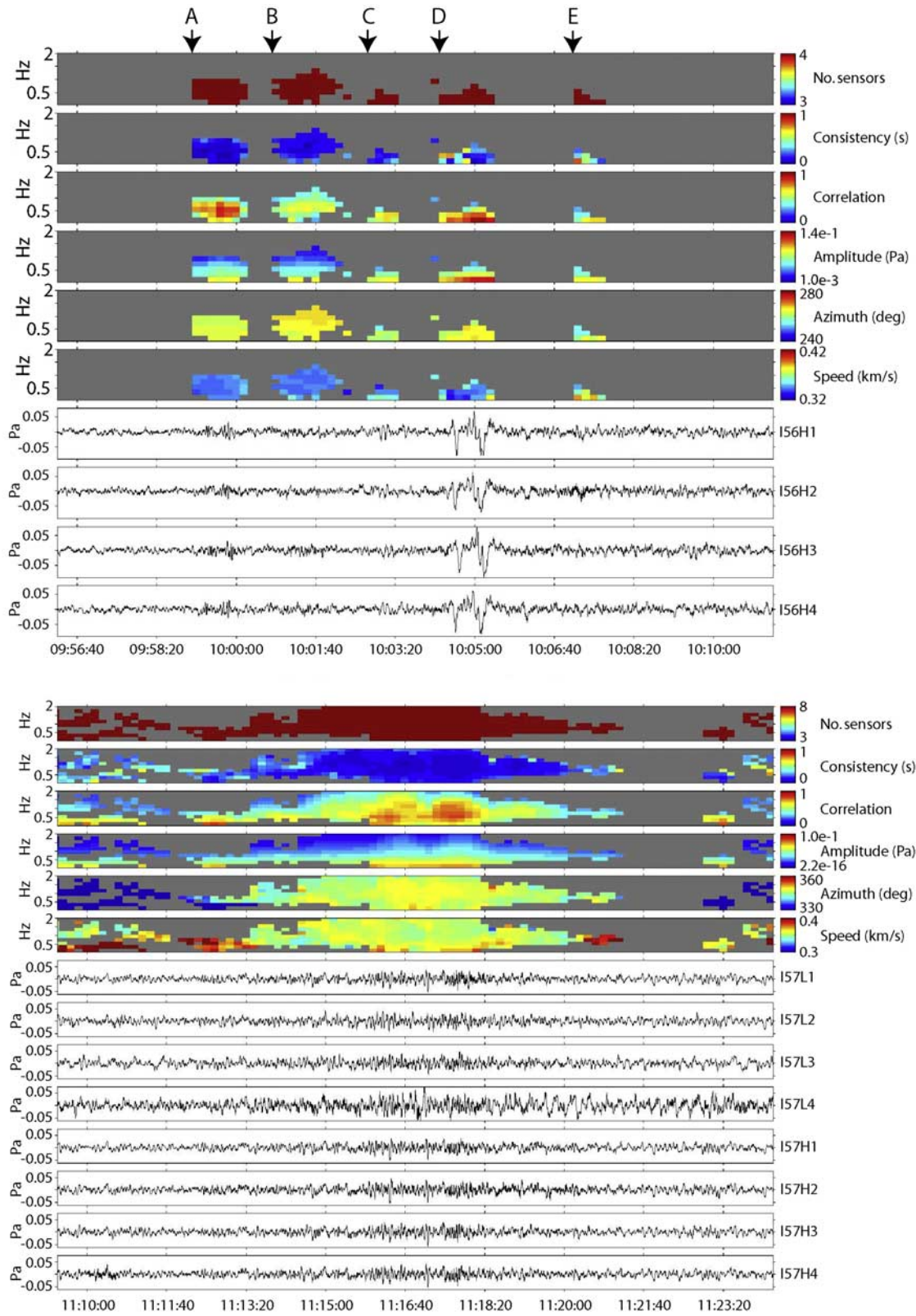


Figure 4. Acoustic signals from the Washington State bolide recorded at I56US (top) and I57US (bottom). In each plot, colored panels display various parameters associated with detections from array processing the data using the PMCC algorithm. Five distinct arrivals at I56US are labeled. At I57US, we cannot resolve separate arrival packets.

Table 3. Main Characteristics of the Infrasound Signals Generated by the Washington State Bolide

Stations	Duration (min)	Maximum Amplitude (Pa)	Frequency Content (Hz)	Azimuth Range (°)	Trace Velocity (km/s)
I56US	8.5	0.17	0.469 ± 0.333	263 ± 2.8	0.346 ± 0.011
I57US	9	0.1	1.003 ± 0.546	345.7 ± 2.5	0.356 ± 0.012

~11:16 and 11:19. Preceding and following the highly coherent signal from the bolide are low-amplitude detections caused by surf offshore Southern California. We observe 10,000's of such signals at the I57US array annually [Arrowsmith and Hedlin, 2005]. The signal from the bolide can be easily separated from the surf infrasound as it comes from a different backazimuth.

5. Forward Modeling

5.1. Background Atmospheric Specifications

[20] Profiles of temperature, wind speed, and wind direction are extracted from the G2S model (described above)

along the great circle paths from source to receiver (for both I56US and I57US), constituting a two-dimensional range-dependent Cartesian coordinate system. The great circle path is approximated for a spherical earth with an average radius of 6378.206 km. Deviations from the true great circle path that account for the Earth's oblateness are negligible in the context of the uncertainties of the atmospheric data and the propagation model physics. A total of 325 and 1494 range steps (for I56US and I57US, respectively) at 0.01° intervals (~1.1 km) is provided in the horizontal direction, while 801 vertical steps at 0.25 km interval from mean sea level to the thermosphere are provided in the vertical

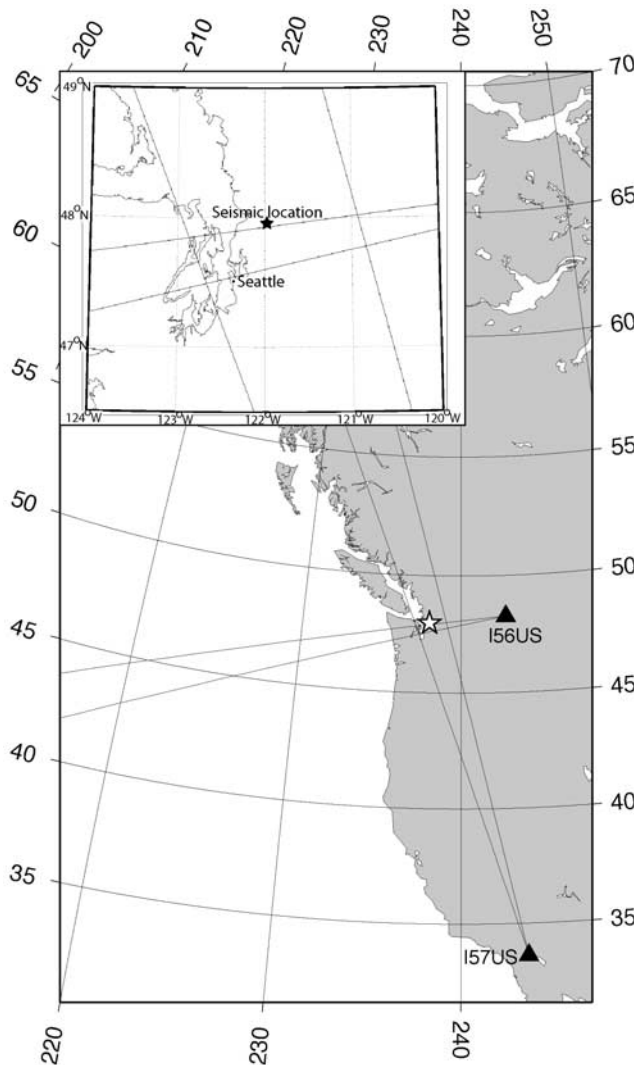


Figure 5. Stereographic equal area projection showing the seismically derived location (star), locations of infrasound arrays (triangles), and their corresponding maximum and minimum azimuths of signals from the Washington bolide. Inset: zoom on the source location.

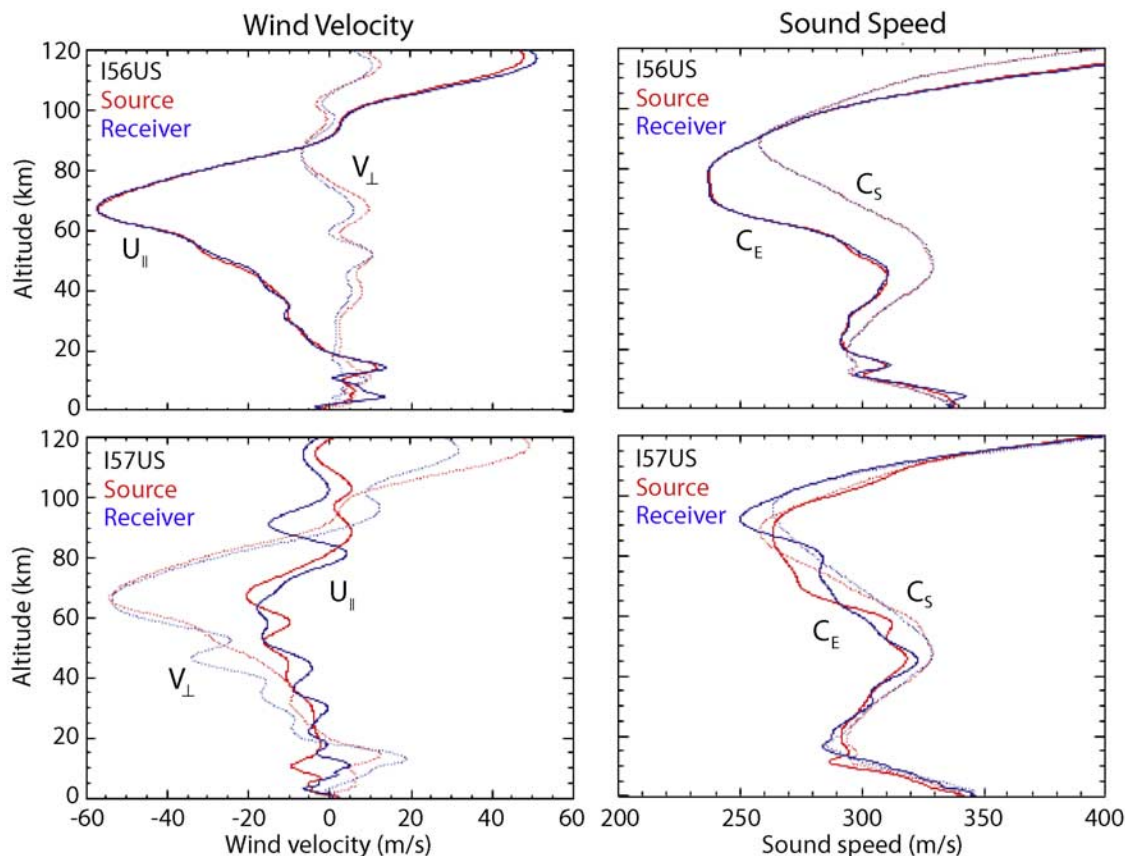


Figure 6. Environmental profiles of wind velocity (left column) and along track (u_{\parallel}) and cross-track (v_{\perp}) wind components of the sound speed (right column) from the seismically derived source location to the I56US array (top row) and I57US array (bottom row).

direction. These resolutions, which are oversampled relative to the resolution of the input data source, allow for the efficient calculation of range-dependent parabolic equation models. Atmospheric pressure (P) and total mass density (ρ) from the G2S model are used to calculate the static sound speed at all points along the two-dimensional path from the relation $c = \sqrt{(\gamma P/\rho)}$, with $\gamma = 1.4$. The zonal (u) and meridional (v) wind components from the G2S model were projected into along track (u_{\parallel}) and cross-track (v_{\perp}) wind components using the relations $u_{\parallel} = u \cos(\theta) + v \sin(\theta)$ and $v_{\perp} = -u \sin(\theta) + v \cos(\theta)$ with $\theta = 90 - \phi$, where ϕ is the navigational bearing at each point along the propagation path. The environmental profiles from the estimated terminal burst of the bolide to the I56US and I57US arrays are shown in Figure 6.

[21] One of the goals of this research investigation is to demonstrate that specular reflection off terrain gradients should not be ignored in mountainous regions. Therefore in addition to the atmospheric specifications, terrain elevation estimates at $30'$ resolution (1 km) are provided along the great circle path with new capabilities built into the G2S system. The NOAA Global Land One-km Base Elevation (GLOBE) digital terrain model provides the underlying data [Hastings and Dunbar, 1998]. At 1-km resolution, deviations of the actual elevation along the true great circle path become comparable, but again relative to uncertainties in

the atmospheric specifications and propagation physics, the general assumptions made to specify the lower boundary conditions are reasonable.

5.2. Propagation Models

[22] There are several propagation modeling techniques available to simulate and develop understanding of the infrasonic observables from the Washington State bolide event. Ray-tracing algorithms provide perhaps the easiest way to calculate signal traveltimes and azimuth deviations. Using a “shooting method” the eigenrays for a given source to receiver configuration and background atmosphere can be calculated in a timely manner. The various levels of model sophistication range from a fully range-dependent calculation in spherical coordinates, such as provided the HARPA model [e.g., Jones *et al.*, 1986], to two-dimensional range-independent calculations in Cartesian coordinates [e.g., Garces *et al.*, 1998; Drob *et al.*, 2003].

[23] Another wave propagation modeling approach that can be used to supplement ray trace calculations is the parabolic equation (PE) methodology. This method is primarily used to calculate signal strength loss estimates at a particular frequency assuming a continuous wave source. These models integrate a parabolic approximation to the wave equation in the two-dimensional plane from

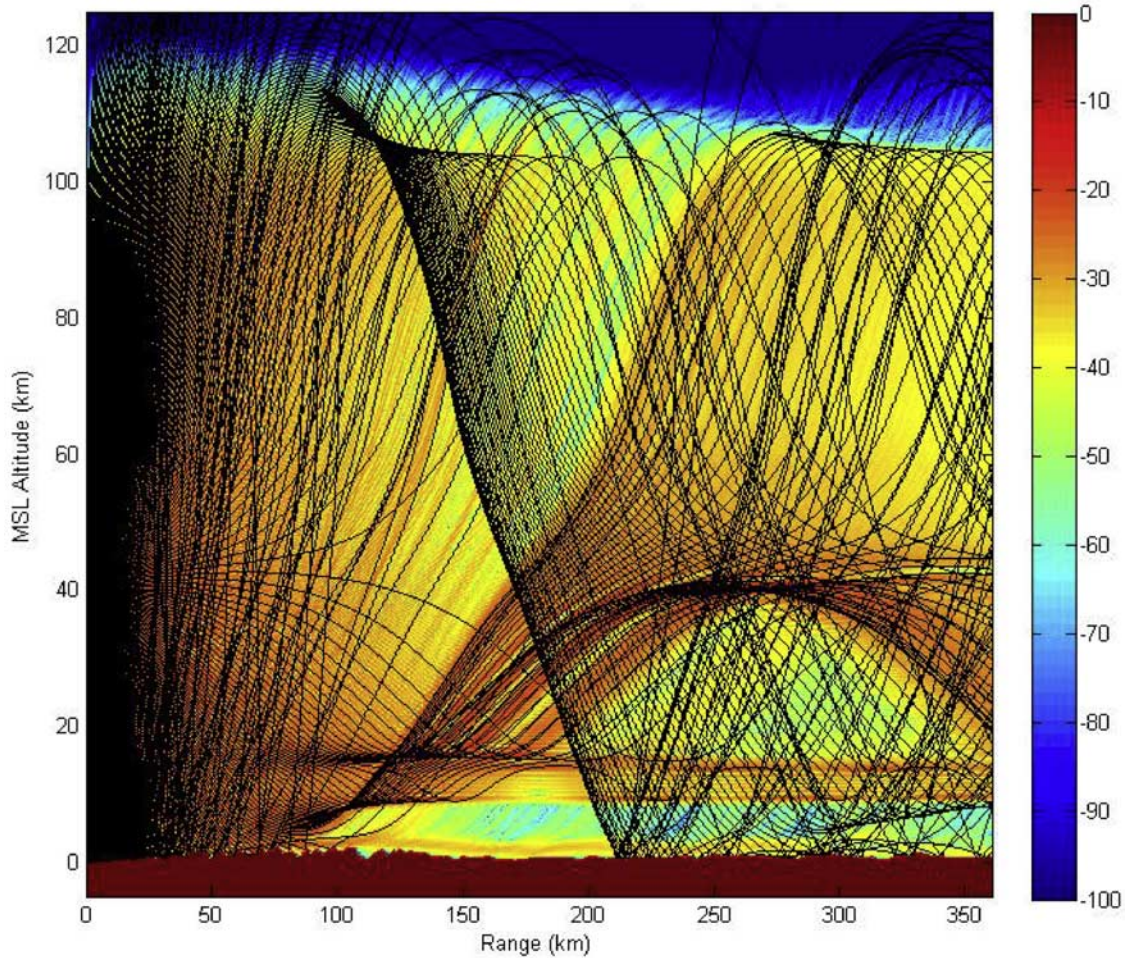


Figure 7. Results from forward modeling calculations from the source location (as located seismically) to I56US. Black lines show raypaths obtained from ray shooting. The background color scale shows amplitudes from parabolic equation calculations at 1 Hz. “MSL Altitude” refers to the altitude above mean sea level.

source to receiver, accounting for frequency-dependent molecular attenuation, radial spreading losses, nonlinear wind shear terms, range-dependent environmental conditions, and variable terrain. These calculations typically ignore cross-track winds and out of plane surface scattering. Parabolic equation modeling overcomes several of the limitations of ray methods that include validity in the high-frequency limit, the inability of ray-based methods to easily estimate signal altitudes near caustics, and the numerical sensitivity near turning points. However, the computation of traveltimes with PE algorithms involves costly broadband calculations over a range of frequencies, which are required in order to perform a Fourier waveform synthesis. In addition, PE codes have difficulties in calculating azimuth “wavefront” arrival angles or azimuth deviations, which can be approximately 5° , as the result of cross-track winds. Thus, ray calculations remain the dominant approach in the arena of source location and infrasound event analysis applications.

[24] To model the observed infrasound signals at I56US and I57US, we utilize the NRL RAMPE code of *Lingevitch et al.* [2002], as well as a simple (yet

robust) range-dependent two-dimensional Cartesian ray trace code. The RAMPE code utilizes the attenuation coefficients of *Sutherland and Bass* [2004]. Both calculations are computed on the Cartesian plane along a great circle path from source to receiver and account for range-dependent variations of the background fields as well as terrain and gradient effects. The PE calculations ignore the effects of cross-track wind and gradient terms, as well as oblique (out of plane) topographic reflections.

[25] The underlying equations for range-dependent ray tracing in a three-dimensional, spatially varying, windy atmosphere are given by *Lighthill* [1978] (e.g., equations (148) and (149)). Reproduced here, they are

$$\begin{aligned} \frac{dx_i}{dt} &= V_i + \frac{\partial \omega_r}{\partial k_i}, \quad \frac{dk_i}{dt} = k_j \frac{\partial V_j}{\partial x_i} + \frac{\partial \omega_r}{\partial k_i}, \quad \omega \\ &= kV_j(x_1, x_2, x_3) + \omega_r(k_1, k_2, k_3, x_1, x_2, x_3), \quad \omega_r \\ &= c_o(k_1^2 + k_2^2 + k_3^2), \end{aligned}$$

where x_i is the Cartesian coordinate of the ray, k_i is the wave number vector, V_i is the wind velocity component, c_o is the static sound speed, and ω_r is the relative frequency.

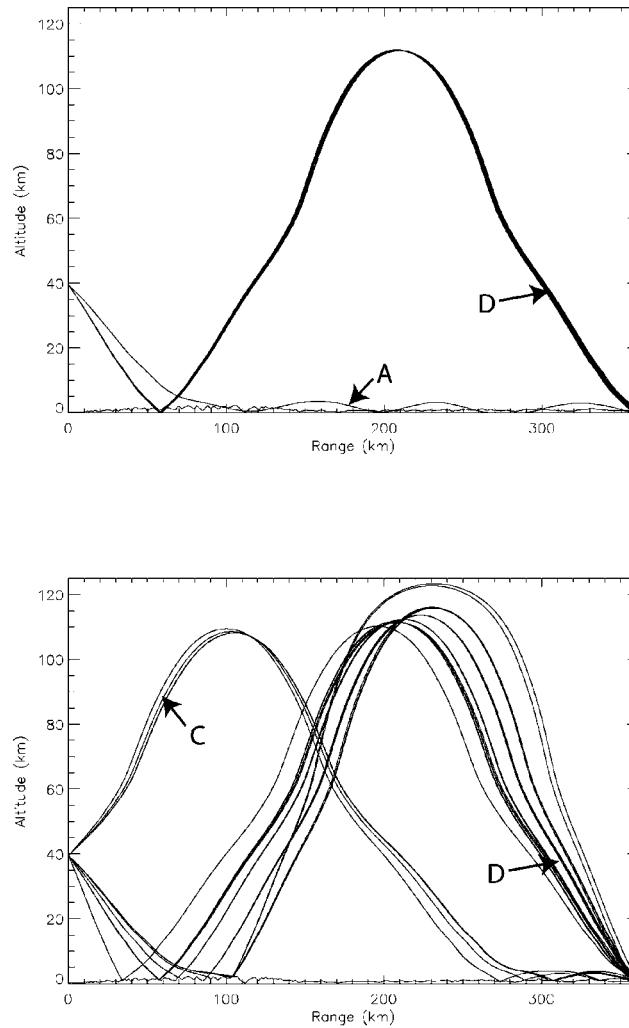


Figure 8. Raypath solutions obtained that connect the source location to I56US with no topography used in the calculation (top) and including topography (bottom). Topography is also plotted in each panel.

[26] It is well known that the general characteristics of infrasound propagation are largely determined by the vertical structure of the atmosphere. For typical atmospheric conditions, the vertical gradient terms (dc/dx_3 and dV/dx_3) are typically an order of magnitude greater than the horizontal terms. Thus, in certain circumstances range-independent propagation calculations can often be used to quickly calculate reasonably accurate results. It should be noted that range independence may also be generally appropriate for surface temperature inversions and Lamb wave propagation calculations in some cases. Range independence is generally applicable to distances of approximately 300–600 km (typical thermospheric and stratospheric first and second bounce distances). The assumption of range independence is not valid in cases where strong meteorological gradients exist, such as near the boundaries of the tropospheric jet stream or in the vicinity of severe weather fronts.

6. Modeling Results

[27] In numerically modeling the propagation of infrasound from the terminal burst of the bolide to I56US and

I57US, we have been able to successfully simulate most of the separate arrivals at I56US but have had greater difficulty in reproducing the observations at I57US. Our results are documented for each array separately.

6.1. IS56US

[28] We have been able to successfully model and explain the traveltimes for three of the four (and possibly five) distinct arrival packets at I56US (Figures 7 and 8). The group of arrivals at 10:05, which contains several large amplitude peaks, can be explained by thermospherically ducted rays that first strike the ground ('D' in Figures 4 and 8). The third packet of energy at 10:03 ('C' in Figures 4 and 8) can be explained by upward launched thermospherically ducted rays, being converted to tropospherically ducted rays by specular reflection off the downslope of mountains west of the receiver. Successfully modeling the first arrival at ~09:58 ('A' in Figure 4) proved to be more problematic. While the full wave PE calculations (Figure 7) clearly indicate a narrow acoustic duct in the first 5 km above the ground, the ray code was only able to find a ray solution along this path by neglecting the terrain reflection effects. By

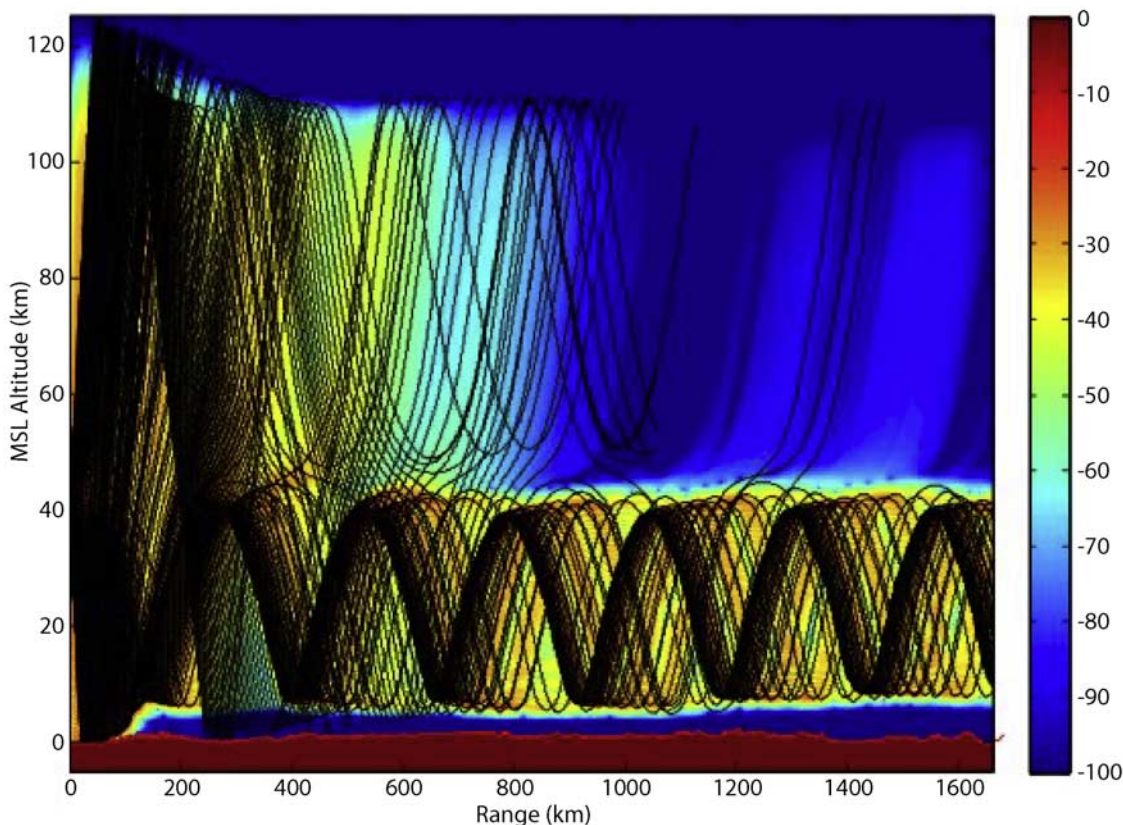


Figure 9. Results from forward modeling calculations from the source location (as located seismically) to I57US. Black lines show raypaths obtained from ray shooting. The background color scale shows amplitudes from parabolic equation calculations at 1 Hz. “MSL Altitude” refers to the altitude above mean sea level.

neglecting the terrain elevation and gradient reflection effects for this one raypath, the traveltimes for the eigen solutions matched the observed traveltimes of the first arrival extremely well. We are unable to explain the second packet of energy at 10:01 (‘B’ in Figure 4) with our eigenray solver. However, it is important to note that we only included terrain gradient reflection effects in the along-track direction and that we neglected oblique gradient reflection effects in order to limit computational complexity in both PE and ray simulations.

[29] This is a unique result as we have been able to explain a sequence of separate arrivals by multipathing from the same source location. This result clearly illustrates the complexity associated with modeling infrasound propagation, yet we have been able to accurately predict much of the structure in the waveforms observed at I56US.

6.2. IS57US

[30] Despite our success in modeling the propagation of infrasound to I56US, we have been unable to satisfactorily explain the signals observed at I57US using the same suite of models (Figure 9). This is an important result and illustrates some of the limitations in our current ability to model infrasonic propagation. A likely factor contributing to our inability to successfully explain the observations is the longer signal propagation path to I57US (at a distance of ~ 1659 km), which makes it more likely that errors in the background field, source location, and propagation physics will compound or amplify to result in appreciable discre-

pancies between the model predictions and observations. Multiple simulations assuming reasonably simple statistical perturbations to the source altitude and atmospheric conditions are unable to satisfactorily explain the I57US arrival times in a repeatable manner. This inability points to the need to continue evaluating current modeling capacities with data from other infrasound ground-truth events. Such analyses should help improve the current scientific understanding of infrasound propagation physics and of the upper atmosphere.

[31] There are several possible reasons for our inability to successfully model the observations at I57US at this time. First, the signal could be from the hypersonic shock wave of the bolide rather than the terminal burst (as appears to be observed at I56US). This could explain the long continuous signal observed at I57US (~ 8 min duration). Unfortunately, we have been unable to obtain reliable ground-truth information on the bolide path. However, the seismic data imply that the acoustic signal is associated with the terminal burst of the event. Furthermore, the long-duration signal observed at I57US could also be caused by the superposition of multiple paths of acoustic energy through the atmosphere.

[32] A second possibility is that the energy detected at I57US escaped from the elevated stratospheric duct through wave scattering effects that have been unaccounted for (Figure 9). For example, the observed horizontal trace velocity is consistent with a typical stratospheric return

[Cepilecha *et al.*, 1998]. This hypothesis is further supported by the fact that the signal maintained its high-frequency content and appreciable power above 1 Hz over a distance of >1600 km. Arguments against significant leaking or scattering from the elevated stratospheric duct are supported by the depth of the sound channel illustrated by the ray and PE calculations in Figure 9. Even though the G2S model is averaged to about 100 km horizontal resolution, it is very unlikely that unresolved finer-scale “holes” in the waveguide could exist, which would however allow for direct leakage of energy to the surface to occur. Such structures would violate basic atmospheric dynamic stability considerations. However, the observed range variations in the environmental conditions from source to receiver do not rule out (and possibly even support) the hypothesis of nonlinear normal mode hopping and dispersion effects that could result in detectable signal amplitudes at I57US. Further exploration with a fully resolved, time- and range-dependent, nonlinear infrasound wave propagation technique is needed.

[33] A third possibility is that the observed infrasonic signals were thermospherically ducted. Given the current G2S specifications of the 80- to 120-km altitude range, this would seem very unlikely as the predicted thermospheric eigenray paths (not shown in Figure 9) involve as many as five to six surface reflections, have ray turning points exceeding 110–115 km, and traveltimes in excess of 100 s of the observed values. Such ray turning points would be in contradiction with the observation of appreciable acoustic wave power above 1 Hz over distances of >1600 km from the source.

[34] Given this evidence, then perhaps the most likely reason for a difference between modeled results and observations is the possibility of a gross underestimation of the lower thermospheric and upper mesospheric meridional wind for this event. An increased meridional wind velocity would imply that the upper limit of the thermospheric duct occurs at a much lower altitude than predicted, leading to shorter traveltimes and less molecular attenuation. Furthermore, this explanation is supported by a growing wave of evidence that the HWM-93 model does in fact significantly underestimate the amplitude of the migrating diurnal and semidiurnal tidal components in the mesosphere and lower thermosphere for certain latitudes regions and seasons [e.g., Burrage *et al.*, 1993; Hagan and Forbes, 2002; Le Pichon *et al.*, 2005]. This explanation could also help to explain the relatively low horizontal trace velocity observed, which is more indicative of a stratospheric return.

7. Conclusions

[35] The Washington State bolide is by far one of the most seismically well-recorded bolides to date, in part due to the proximity of its terminal burst to one of the most densely monitored areas in North America. Infrasonic signals from the bolide were also clearly observed at two IMS infrasound arrays (located at ranges of 363 and 1659 km from the terminal burst of the bolide). This unprecedented data set has allowed us the opportunity to obtain a highly accurate seismic location with a very small lateral uncertainty (Table 2). Taking the seismically derived location as effective ground-truth, we have used this event to

test existing atmospheric models and propagation codes in order to assess how successfully we are able to predict the complexity of the acoustic waveforms observed at the two infrasound arrays. The results for I56US related range-dependent ducting and specular reflection off nearby mountains to successfully explain the majority of the separate arrival packets. This is the first time to our knowledge that this has been observed and successfully predicted for such an event. Our results build on previous studies that have looked at the complex generation of infrasonic signals by the vertical forcing of mountain ranges by large earthquakes [Olson *et al.*, 2003; Le Pichon *et al.*, 2002b]. At the time of writing, we are planning to perform a broadband Fourier waveform synthesis calculation using the NRLRAMPE code to further support these results and possibly better resolve and explain the observed arrival structure at I56US, particularly the primary arrival and unexplained arrivals (‘A’ and ‘B’ in Figure 4). Disappointingly, we were unable to model the signals observed at I57US. As such, this event illustrates some of the current limitations of infrasonic propagation modeling. This event presents an important and open scientific challenge to successfully explain and model the observed signal at I57US. Overall, this study documents an excellent example of a ground-truth event that can be used for evaluating existing atmospheric models and propagation codes. We have successfully modeled multipath energy from a single source to a receiver and illustrated some of the challenges that still need to be faced.

[36] **Acknowledgments.** Approved for Public Release (SMDC); distribution unlimited. We would like to thank John Cassidy (NRCAN) and Steve Malone (University of Washington) for their assistance in identifying the observing seismic stations to this event. We would like to thank Joseph Lingeitch and Geoffrey Edelman for their roles in developing, applying, and refining the NRLRAMPE code for this research. We thank Gene Herrin for reviewing an earlier version of this draft. The PMCC algorithm was provided by Alexis Le-Pichon. The Incorporated Research Institutions for Seismology (IRIS) and the Natural Resources Canada (NRCAN) provided access to the digital seismic waveform data.

References

- Anglin, F., and R. A. W. Haddon (1987), Meteoroid sonic shock-wave-generated seismic signals observed at a seismic array, *Nature*, *328*, 607–609.
- Arrowsmith, S. J., and M. A. H. Hedlin (2005), Observations of infrasound from surf in Southern California, *Geophys. Res. Lett.*, *32*, L09810, doi:10.1029/2005GL022761.
- Bloom, S., et al. (2005), Documentation and validation of the Goddard Earth Observing System (GEOS) Data Assimilation System-Version 4, *TM-2005-104606*, NASA Goddard Space Flight Center, Greenbelt, Md.
- Brown, P. G., R. W. Whitaker, D. O. Revelle, and E. Tagliarferri (2002), Multi-station infrasonic observations of two large bolides: Signal interpretation and implications for monitoring of atmospheric explosions, *Geophys. Res. Lett.*, *29*(13), 1636, doi:10.1029/2001GL013778.
- Brown, P. G., P. Kalenda, D. O. Revelle, and J. Borovicka (2003), The Moravka meteorite fall: 2. Interpretation of infrasonic and seismic data, *Meteorit. Planet. Sci.*, *38*, 989–1003.
- Brown, P. G., D. Pack, W. N. Edwards, D. O. ReVelle, B. B. Yoo, R. E. Spalding, and E. Tagliarferri (2004), The orbit, atmospheric dynamics and initial mass of the Park Forest meteorite, *Meteorit. Planet. Sci.*, *39*, 1781–1796.
- Burrage, M. D., et al. (1993), Comparison of HRDI wind measurements with radar and rocket observations, *Geophys. Res. Lett.*, *20*, 1259–1262.
- Cansi, Y. (1995), An automated seismic event processing for detection and location: The P.M.C.C. method, *Geophys. Res. Lett.*, *22*, 1021–1024.
- Cates, J. E., and B. Sturtevant (2002), Seismic detection of sonic booms, *J. Acoust. Soc. Am.*, *111*, 614–628.
- Cepilecha, Z., J. Borovicka, W. G. Elford, D. O. Revelle, R. L. Hawkes, V. Porubcan, and M. Simek (1998), Meteor phenomena and bodies, *Space Sci. Rev.*, *84*, 327–471.

- Drob, D. P. (2004), Atmospheric specifications for infrasound calculations, *InfraMatics*, 5, 6–13.
- Drob, D. P., J. M. Picone, and M. A. Garcés (2003), The global morphology of infrasound propagation, *J. Geophys. Res.*, 108(D21), 4680, doi:10.1029/2002JD003307.
- Edwards, W. N., and A. R. Hildebrand (2004), SUPRACENTER: Locating fireball terminal bursts in the atmosphere using seismic arrivals, *Meteorit. Planet. Sci.*, 39, 1449–1460.
- Evers, L. G., and H. W. Haak (2001), Listening to sounds from an exploding meteor and oceanic waves, *Geophys. Res. Lett.*, 28, 41–44.
- Evers, L. G., and H. W. Haak (2003), Tracing a meteoric trajectory with infrasound, *Geophys. Res. Lett.*, 30(24), 2246, doi:10.1029/2003GL017947.
- Garcés, M. A., R. A. Hansen, and K. G. Lindquist (1998), Traveltimes for infrasonic waves propagating in a stratified atmosphere, *Geophys. J. Int.*, 135, 255–263.
- Hagan, M. E., and J. M. Forbes (2002), Migrating and nonmigrating diurnal tides in the middle and upper atmosphere excited by tropospheric latent heat release, *J. Geophys. Res.*, 107(24), 4754, doi:10.1029/2001JD001236.
- Hastings, D. A., and P. K. Dunbar (1998), Development and assessment of the Global Land One-km Base Elevation Digital Elevation Model (GLOBE), paper presented at the International Society for Photogrammetry and Remote Sensing Commission IV Symposium, Stuttgart, Germany, 7–10 Sept.
- Hedin, A. E., et al. (1996), Empirical wind model for the upper, middle, and lower atmosphere, *J. Atmos. Terr. Phys.*, 58, 1421–1447.
- Hedlin, M. A. H., G. Alcoverro, and G. D’Spain (2003), Evaluation of rosette infrasonic noise-reducing spatial filters, *J. Acoust. Soc. Am.*, 114, 1807–1820.
- Ishihara, Y., S. Tsukada, S. Sakai, Y. Hiramatsu, and M. Furumoto (2003), The 1998 Miyako fireball’s trajectory determined from shock wave records of a dense seismic array, *Earth Planets Space*, 55, e9–e12.
- Ishihara, Y., F. Muneyoshi, S. Sakai, and S. Tsukada (2004), The 2003 Kanto large bolide’s trajectory determined from shockwaves recorded by a seismic network and images taken by a video camera, *Geophys. Res. Lett.*, 31, L14702, doi:10.1029/2004GL020287.
- Jones, M. J., J. P. Riley, and T. M. Georges (1986), A versatile three-dimensional Hamiltonian ray-tracing program for acoustic waves in the atmosphere above irregular terrain, *NOAA special report*, Wave propagation Laboratory, Boulder, Colo.
- Kalnay, E., M. Kanamitsu, and W. E. Baker (1990), Global numerical weather prediction at the National Meteorological Center, *Bull. Am. Meteorol. Soc.*, 71, 1410–1428.
- Kanamitsu, M. (1989), Description of the NMC global data assimilation and forecast system, *Weather Forecast.*, 4, 335–342.
- Langston, C. A. (2004), Seismic ground motions from a bolide shock wave, *J. Geophys. Res.*, 109, B12309, doi:10.1029/2004JB003167.
- Le Pichon, A., J. M. Guerin, E. Blanc, and D. Reymond (2002a), Trail in the atmosphere of the 29 December 2000 meteor as recorded in Tahiti: Characteristics and trajectory reconstruction, *J. Geophys. Res.*, 107(D23), 4709, doi:10.1029/2001JD001283.
- Le Pichon, A., J. Guilbert, A. Vega, M. Garces, and N. Brachet (2002b), Ground-coupled air-waves and diffracted infrasound from the Arequipa earthquake of June 23, 2001, *Geophys. Res. Lett.*, 29(18), 1886, doi:10.1029/2002GL015052.
- Le Pichon, A., E. Blanc, and D. Drob (2005), Probing high-altitude winds using infrasound, *J. Geophys. Res.*, 110, D20104, doi:10.1029/2005JD006020.
- Lighthill, J. (1978), *Waves in Fluids*, Cambridge University Press, New York, NY.
- Lingevitch, J. F., M. D. Collins, and M. J. Mills (2002), A two-way parabolic equation that accounts for multiple scattering, *J. Acoust. Soc. Am.*, 112, 476–480.
- McIntosh, B. A. (1970), On the end-point height of fireballs, *J. R. Astron. Soc. Can.*, 64, 267–281.
- Olson, J. V., C. R. Wilson, and R. A. Hansen (2003), Infrasound associated with the 3 November, 2002 Denali Fault, Alaska earthquake, *Geophys. Res. Lett.*, 30(23), 2193, doi:10.1029/2003GL018568.
- Picone, J. M., A. E. Hedin, D. P. Drob, and A. C. Aikin (2002), NRLMSISE-00 Empirical model of the atmosphere: Statistical comparisons and scientific issues, *J. Geophys. Res.*, 107(A12), 1468, doi:10.1029/2002JA009430.
- Qamar, A. (1995), Space shuttle and meteoroid-tracking supersonic objects in the atmosphere with seismographs, *Seismol. Res. Lett.*, 66, 6–12.
- Revelle, D. O. (1976), On meteor-generated infrasound, *J. Geophys. Res.*, 81, 1217–1230.
- Sutherland, L. C., and H. E. Bass (2004), Atmospheric absorption in the atmosphere up to 160 km, *J. Acoust. Soc. Am.*, 115, 1012–1032.

S. J. Arrowsmith, Los Alamos National Laboratory, EES-2, P. O. Box 1663, MS D401, Los Alamos, NM 87545, USA. (sarrowsmith@gmail.com)

D. P. Drob, U.S. Naval Research Laboratory, 4555 Overlook Avenue, Washington, DC 20375, USA.

W. Edwards, Department of Earth Sciences, University of Western Ontario, London, Ontario, Canada N6A 5B7.

M. A. H. Hedlin, Institute of Geophysics and Planetary Physics, Scripps Institution of Oceanography, University of California, San Diego, CA 92093-0225, USA.